molecular pharmaceutics

Article

pubs.acs.org/molecularpharmaceutics

Folate Receptor-Targeted Multimodality Imaging of Ovarian Cancer in a Novel Syngeneic Mouse Model

Meltem Ocak,[†,○] Andrea G. Gillman,[‡,○] Jamee Bresee,[†,○] Lixin Zhang,[§] Anda M. Vlad,[§,∥] Cristina Müller,[▽] Roger Schibli,[▽] W. Barry Edwards,[†,‡] Carolyn J. Anderson,[†,‡,⊥,#] and H. Michael Gach*[,†,‡,#]

[†]Department of Radiology, [‡]Cancer Institute, [§]Department of Obstetrics, Gynecology & Reproductive Sciences, [∥]Magee Womens Research Institute, [⊥]Department of Pharmacology & Chemical Biology, [#]Department of Bioengineering, University of Pittsburgh, Pittsburgh, Pennsylvania 15213, United States

[▽]Center for Radiopharmaceutical Sciences ETH-PSI-USZ, Paul Scherrer Institute, 5232 Villigen-PSI, Switzerland

Supporting Information

ABSTRACT: A new transplantable ovarian tumor model is presented using a novel folate receptor (FR) positive, murine ovarian cancer cell line that emulates the human disease and induces widespread intraperitoneal (i.p.) tumors in immunocompetent mice within 4−8 weeks of implantation. Tumor development was monitored using a new positron emission tomography (PET) FR-targeting reporter with PET/computerized tomography (PET/CT) and fluorescence molecular tomography (FMT) using a commercial FR-targeting reporter. Conventional structural magnetic resonance imaging (MRI) was also performed. Adult female C57BL/6 mice were injected i.p. with 6×10^6 MKP-L FR+ cells. Imaging was performed weekly beginning 2 weeks after tumor induction. The albumin-binding, FR-targeting ligand cm09 was radiolabeled with the positron emitter ^{68}Ga and used to image the tumors with a small animal PET/CT. The FR-reporter FolateRSense 680 (PerkinElmer) was used for FMT and flow cytometry. Preclinical MRI (7 T) without FR-targeting was compared with the PET and FMT molecular imaging. Tumors were visible by all three imaging modalities. PET/CT had the highest imaging sensitivity at 3−3.5 h postadministration (mean %IA/g mean > 6) and visualized tumors earlier than the other two modalities with lower kidney uptake (mean %IA/g mean < 17) than previously reported FR-targeting agents in late stage disease. FMT showed relatively low FR-targeted agent in the bladder and kidneys, but yielded the lowest anatomical image resolution. MRI produced the highest resolution images, but it was difficult to distinguish tumors from abdominal organs during early progression since a FR-targeting MRI reporter was not used. Nevertheless, there was good correlation of imaging biomarkers between the three modalities. Tumors in the mouse ovarian cancer model could be detected using FR-targeted imaging as early as 2 weeks post i.p. injection of tumor cells. An imaging protocol should combine one or more of the modalities, e.g., PET/CT or PET/MRI for optimal tumor detection and delineation from surrounding tissues.

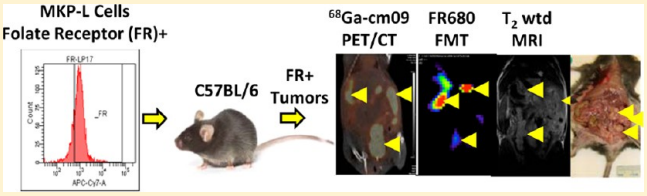

KEYWORDS: *folate receptor targeting, immunocompetent ovarian cancer mouse model, PET/CT, MRI, fluorescence molecular tomography, FolateRSense, cm09, ^{68}Ga*

INTRODUCTION

Epithelial ovarian cancer (EOC) has the highest mortality rate among gynecologic malignancies in the USA and Europe.[1] Because of nonspecific symptoms and lack of effective screening, EOC is usually diagnosed at late stages, when the tumor has spread within the peritoneal cavity. For patients diagnosed at an advanced stage, the 5-year survival rate is under 30%. In contrast, when diagnosed with "low volume," localized, early stage disease, the survival rate is greater than 90%.[2] Progress in early diagnosis, improved therapeutic success against the primary tumor, and increased ability to prevent or lower rates of recurrence depend in part on the development of useful preclinical animal (e.g., mouse) models that mirror the tumor biology seen in humans.

Traditionally, subcutaneous (s.c.) and intraperitoneal (i.p.) tumor xenografts in immunodeficient nude mice were used as a model system. However, tumor growth and treatment in these models are affected by immune system deficiencies.[3] The syngeneic, immunocompetent orthotopic model system provides an alternative and potentially more appropriate ovarian cancer model for studies on pathogenic mechanisms and preclinical testing of new therapies.[4] Several genetically engineered mouse models were developed during the past decade, incorporating genetic mutations often observed in

Received: September 18, 2014
Revised: November 21, 2014
Accepted: December 23, 2014
Published: December 23, 2014

DOI: 10.1021/mp500628g
Mol. Pharmaceutics 2015, 12, 542−553

human disease.[3] Transplantable tumor models whereby tumor cells were injected into immunocompetent mice resulted in widespread peritoneal dissemination that closely resembled the recurrent tumors seen in the human disease.[5] The advent of these mouse models offers opportunities for numerous *in vivo* studies targeting various aspects of disease, ranging from mechanisms of early tumor development to pharmacological responses to therapy. However, an accurate assessment of the outcome in such studies often requires *in vivo* imaging technologies with adequate specificity and sensitivity.

Magnetic resonance imaging (MRI), positron emission tomography/computerized tomography (PET/CT), optical, single photon emission computed tomography (SPECT), and ultrasound are used in both preclinical and clinical applications for the detection and characterization of EOC. Molecular imaging of EOC through various biomarkers will yield information at the molecular and cellular level of the disease. One such biomarker for EOC is folate receptor (FR) alpha (FRα). FRα expression is known to be highly elevated in 75−85% of epithelial ovarian tumors when compared to normal tissues with the exception of the kidneys and choroid plexus.[6−8] Therefore, FRα is a prime target for diagnostic imaging and therapeutic interventions in EOC. Current FR-targeting strategies include the use of anti-FRα antibodies or folic acid conjugates to imaging agents, therapeutic compounds, T cells, nanoparticles, and oncolytic viruses.[9−16]

FR-targeting imaging tracers were successfully developed and tested *in vivo* during the past decade. The SPECT tracer FolateScan (^{99m}Tc-EC20, Endocyte) is used in clinical studies for solid tumors with high FR-expression.[17,18] The folate conjugate cm09 includes an albumin-binding entity that increases its serum half-life and a DOTA-chelator that allows radiolabeling with a variety of nuclides for either SPECT or PET imaging, or radionuclide therapy.[19−21] The optical FR-targeting agent FolateRSense 680 (FR680, PerkinElmer) can be used for both flow cytometry and preclinical imaging. FR-targeting MRI agents based on gadolinium (Gd) or iron oxide were demonstrated, but the inherent tracer sensitivity of MRI is inferior to PET, SPECT, and optical modalities.[22−27]

We report herein a new transplantable ovarian tumor model using a novel FRα+ ovarian tumor cell line, MKP-L. On the basis of this model, we developed and optimized a preclinical FR-targeted imaging protocol for the detection of FRα+ MKP-L tumors in C57BL/6J mice. Tumor-bearing mice were imaged by three separate modalities: PET/CT using the PET agent ^{68}Ga-cm09, optical fluorescence molecular tomography (FMT) using FolateRSense 680, and structural MRI (without FR-targeting). In this animal model, each of the imaging modalities displayed different strengths and weaknesses. These results suggest an optimal imaging protocol and reveal future directions for multimodal ovarian tumor imaging.

EXPERIMENTAL SECTION

***In Vitro* Detection of Folate Receptor on Murine Ovarian Cancer Cells.** The MKP-L cell line was derived from one MUC1KrasPten (MKP) mouse with a late stage, loco-regionally spread, orthotopic ovarian tumor. The MKP preclinical model employs conditional (Cre-loxP) mutations in oncogenic Kras and Pten tumor suppressors. Upon AdCre injection under the ovarian bursa, the MKP mice progress to endometrioid ovarian tumors that spread loco-regionally and are accompanied by ascites accumulation.[28] The MKP-L primary ovarian tumor cells were cultured in complete Dulbecco's modified eagle medium (DMEM, Corning cellgro), containing 10% fetal bovine serum (FBS, 1% nonessential amino acids, 10,000 U/L penicillin, 10,000 μg/mL streptomycin, 2 mM L-glutamine, 1 mM sodium pyruvate, and 0.1 mM 2-mercaptoethanol (all from Sigma-Aldrich, St. Louis, MO).

To identify cell surface FRα expression, MKP-L cells were stained *in vitro* with 600 nM FR680 diluted in phosphate-buffered saline (PBS), according to the manufacturer's instructions. Staining was performed at 37 °C for 1 h, under gentle agitation of the tubes, manually performed every 15 min. Cells were immediately analyzed with an LSRII flow cytometer (BD Biosciences) and FACSDiva software (BD Biosciences). Unstained cells were used for gating strategies. Any cells scattered outside the autofluorescence signal were considered FR+. Total FRα protein expression was also confirmed via Western blot. A total of 2 million MKP-L cells were lysed in 100 μL of 1× sodium dodecyl sulfate (SDS) loading buffer (62.5 mM Tris pH 6.8, 2% SDS, 10% glycerol, 0.1 M dithiothreitol (DTT), and 0.01% bromophenol blue). Twenty microliters of cell lysate were subjected to 4−20% SDS-PAGE and blotted with anti-FRα rabbit polyclonal antibody (Abcam, ab67422) diluted 1:1000 in blocking buffer (5% skim milk with 0.05% Tween-20 in PBS). Blotting was performed overnight at 4 °C. Membranes were developed using goat antirabbit IgG−HRP, 1:3000 (BIO-RAD, #170-6515) and the Immun-Star WesternC kit (Bio-Rad). Images were taken by Chemidoc XRS darkroom system (Bio-Rad).

***In Vivo* Ovarian Tumor Formation.** All procedures complied with the University of Pittsburgh Institutional Animal Care and Use Committee guidelines. Nine to ten week old adult female C57BL/6J mice (Jackson Laboratory, n = 13) were injected i.p. with 6 × 10^6 MKP-L cells in 250 μL of PBS. Tumors were allowed to grow until ascites developed or the mice showed signs of pain and/or distress.

Imaging was performed after implantation to monitor tumor growth using 3 cohorts and 3 tumor-free controls (see Supporting Information). Cohorts 2 (n = 6) and 3 (n = 2), and two mice from Cohort 1 (n = 5) were fed a folate-deficient, low autofluorescence diet (Harlan Teklad TD.01013) *ad libitum* (without succinylsulfathiazole) beginning at tumor induction until euthanasia. The remaining 3 mice (Cohort 1) received folate-deficient diet 24−36 h before and during imaging, and regular chow otherwise. Mice were not completely deprived of folate (either by diet or via endogenous production by gut flora) since long-term folate deprivation alters animal growth and tumor metabolism. When mice were imaged in all modalities in the same week, PET/CT was performed on the first day, followed by MRI on the second day and FMT on the third day to minimize FR saturation by the FR-targeting reporters.

PET/CT. *Gallium-68 (^{68}Ga).* ^{68}Ga ($t_{1/2}$ = 68 min, $E_{average}\beta^+$ = 0.830 MeV, 88%) was obtained from a ^{68}Ge/^{68}Ga generator (1.110 MBq, IGG100, Eckert and Ziegler, Berlin, Germany). All chemicals were purchased from Sigma-Aldrich Chemical Co. (St. Louis, MO), unless otherwise specified. Aqueous solutions were prepared using ultrapure water (resistivity, 18 MΩ).

^{68}Ga Labeling. The ^{68}Ga/^{68}Ge generator was eluted with 5−7 mL of 0.1 M HCl, and the eluate (666−740 MBq) was loaded onto a cation exchange column (Strata-X-C, Phenomenex). ^{68}Ga was eluted with 0.8−1 mL of 0.02 M HCl/98% acetone. DOTA-folate (cm09)[19] was labeled with ^{68}Ga (30−150 MBq, 50−150 μL) in ammonium acetate buffer (100−

DOI: 10.1021/mp500628g
Mol. Pharmaceutics 2015, 12, 542−553

150 μL, 0.1 M, pH 4.0) within 10 min at 90 °C. Quality control was performed by radio reversed-phase high-performance liquid chromatography (RP-HPLC). The radiotracer solutions were prepared for animal studies by dilution with sterile 0.9% NaCl.

Internalization Assay with ^{68}Ga-cm09. The FR-mediated internalization of ^{68}Ga-cm09 was studied for the MKP-L cells. MKP-L cells were cultured in DMEM media supplemented with 10% FBS, 1% penicillin−streptomycin−glutamine (PSG), and 2-mercaptoethanol, and cells were incubated at 37 °C, 5% CO_2. One week before the assay, the cells were cultured in a folate-free cell culture medium FFRPMI (modified RPMI, without folic acid, vitamin B12, and phenol red; Cell Culture Technologies GmbH) supplemented with 10% FBS, 1% PSG, and 2-mercaptoethanol. MKP-L cells were seeded in 12-well plates (500,000 cells in 2 mL of supplemented folate-free medium without 10% FBS per well) to grow for 2 days. On the day of the experiment, half of the wells were incubated for 15, 30, 60, and 120 min at 37 °C with excess folic acid (100 μM) in FFRPMI to block FRs on the surface of the MKP-L cells. ^{68}Ga-cm09 was prepared in high labeling yield and radiochemical purity (>98%) at a specific activity of 12−13 MBq/nmol. Ten minutes after incubation of the cells (half of them with folic acid), ^{68}Ga-cm09 (14 pmol) was added to each well and incubated for 15, 30, 60, and 120 min at 37 °C. At specific time points, MKP-L cells were washed two times with PBS. To assess the internalized fraction, MKP-L cells were washed with a sodium acetate-phosphate buffered saline (NaOAC-PBS) pH 4 to release FR-bound ^{68}Ga-cm09 from the cell surface. The lysis of cells was accomplished by the addition of 0.5% SDS-PBS, which enabled transfer of the cell suspensions into tubes for measurement in a γ-counter. The total protein concentration in the cell lysate was determined using the BCA Protein Assay (Pierce Biotechnology, Rockford, IL). Internalized and surface-bound fractions were expressed as fmol/mg of protein.

PET/CT and Image Analysis. The mice were injected with 100 μL of ^{68}Ga-cm09 (6.5−7.4 MBq, 0.5−0.8 nmol) via tail vein and imaged using an Inveon Small Animal PET/CT (Siemens Molecular Imaging, Knoxville, TN). For tail vein injection and throughout imaging, the mice were anesthetized with 2 to 3% isoflurane under oxygen at a flow rate of 2 L/min. Ten minute static scans were acquired approximately 3 to 3.5 h after ^{68}Ga-cm09 injection using the Inveon PET/CT. The 3−3.5 h timing was based on biodistribution studies we conducted in healthy nude mice that showed stable tissue signal in the liver and kidneys despite the short half-life of ^{68}Ga. ^{68}Ga-cm09 uptake in tumors and other organs (heart, liver, kidneys, bladder, and muscle) was quantified using the image analysis software Inveon Research Workplace (IRW, Siemens Medical Solutions, Malvern, PA, USA). Regions of interest (ROIs) were drawn on the fused PET/CT images. The percentage injected activity per gram (%IA/g) was calculated as ROI activity divided by injected dose multiplied by 100% using the IRW software for quantitative comparison among the images.

A blocking PET/CT imaging study was also conducted to examine the specificity of *in vivo* uptake of ^{68}Ga-cm09. For this experiment, two tumor bearing mice (Cohort 3) were scanned at 6 weeks post-tumor cell injection with ^{68}Ga-cm09 to determine the location of tumors. The following day, ^{68}Ga-cm09 PET/CT imaging was repeated with the same mice preinjected with a blocking dose of excess folic acid (100 μg in 100 μL of PBS for each mouse).

Biodistribution Analysis. Immediately following PET/CT imaging at 7 weeks post-tumor cell injection, 3 mice (Cohort 2) were sacrificed and major organs and tissues (liver, kidneys, lung, spleen, heart, intestine, muscle, and tumors) and blood were collected and weighed. Radioactivity was measured using an automatic WIZARD^2 gamma counter (PerkinElmer, Waltham, MA). The results are presented as %IA/g tissue.

Fluorescence Molecular Tomography (FMT). Mice were injected with 2 nmol FR680 fluorescent imaging agent (PerkinElmer) in 100 μL of sterile PBS/mouse via the lateral tail. Prior to imaging, abdominal and back fur were removed using Nair (Church and Dwight). FMT images were acquired using the 680 nm channel ($\lambda_{excitation}$ = 680 nm; $\lambda_{emission}$ = 700 nm) of a VisEn FMT2500 (PerkinElmer) 6 h after FR680 injection. The mice were anesthetized via isoflurane and oxygen mixture, placed in the imaging cassette (VisEn Medical) and imaged in the supine position. Mice were anesthetized throughout the duration of image acquisition, i.e., 5−8 min, depending on the size of the scan field.

Image Analysis. FMT images were reconstructed with the FMT2500 system software TrueQuant (PerkinElmer). FR680 was precalibrated on the FMT2500. Three-dimensional ROIs were drawn around the whole abdomen region to quantify total FR680 uptake (reported in picomoles). Three mice were used as negative controls (Mouse 14, and Mice 3 and 4 at week 1 before they had detectable tumors). Individual tumor ROIs were drawn utilizing necropsies as a reference. Data are presented as tumor to muscle ratios of fluorescence signal. For overlay images, the fluorescence signal and planar image were mirrored to align with MRI and PET/CT images.

Magnetic Resonance Imaging (MRI). A Bruker 7 Tesla (T) ClinScan system was used for all MRI. An 8.6 cm diameter ^{1}H whole-body radiofrequency volume coil was used for transmission, and a surface receive-only 8 × 1 mouse body volume-array coil was used for reception. The mice were anesthetized via isoflurane and oxygen throughout imaging and monitored using the SAII Model 1030 Small Animal Monitoring and Gating System (Small Animal Instruments, Inc.). The animals were kept warm using a SAII MR-compatible Small Rodent Heater System (Small Animal Instruments, Inc.).

Coronal and axial T_1- (TE = 12 ms, average TR = 850 ms) and T_2-weighted (TE = 56 ms, average TR = 1250 ms) abdominal images were acquired using turbo spin echo (TSE) sequences with an approximate resolution of 0.12 mm × 0.12 mm × 0.9 mm. Respiratory gating was used to minimize motion artifacts in the TSE sequences. Additionally, a 3D fast low angle shot (FLASH) volumetric interpolated breath hold examination (VIBE) sequence was used to image intestinal tissue (TE = 3 ms, TR = 5.8 ms, approximate resolution 0.12 mm × 0.12 mm × 0.8 mm).

After the acquisition of the images described above, the gadolinium-based contrast gadobenate dimeglumine (Multihance, Bracco Imaging) was diluted to 52.9 mg/mL in sterile 0.9% NaCl solution and injected via the lateral tail vein at a dosage of 0.1 mmol/kg (105.8 mg/kg). Additional T_1-weighted coronal and axial images were obtained 30 min and 1 h after contrast injection.

Euthanasia, Tumor Dissection, and Immunohistochemistry. The mice were monitored for the development of ascites as an indicator of tumor growth. When the amount of ascites fluid exceeded 5 mL and/or the mice began to show signs of pain or distress, the mice were sacrificed via CO_2 asphyxiation or cervical dislocation. Tumor tissue was harvested at necropsy and immediately placed in 10% formalin, followed

DOI: 10.1021/mp500628g
Mol. Pharmaceutics 2015, 12, 542−553

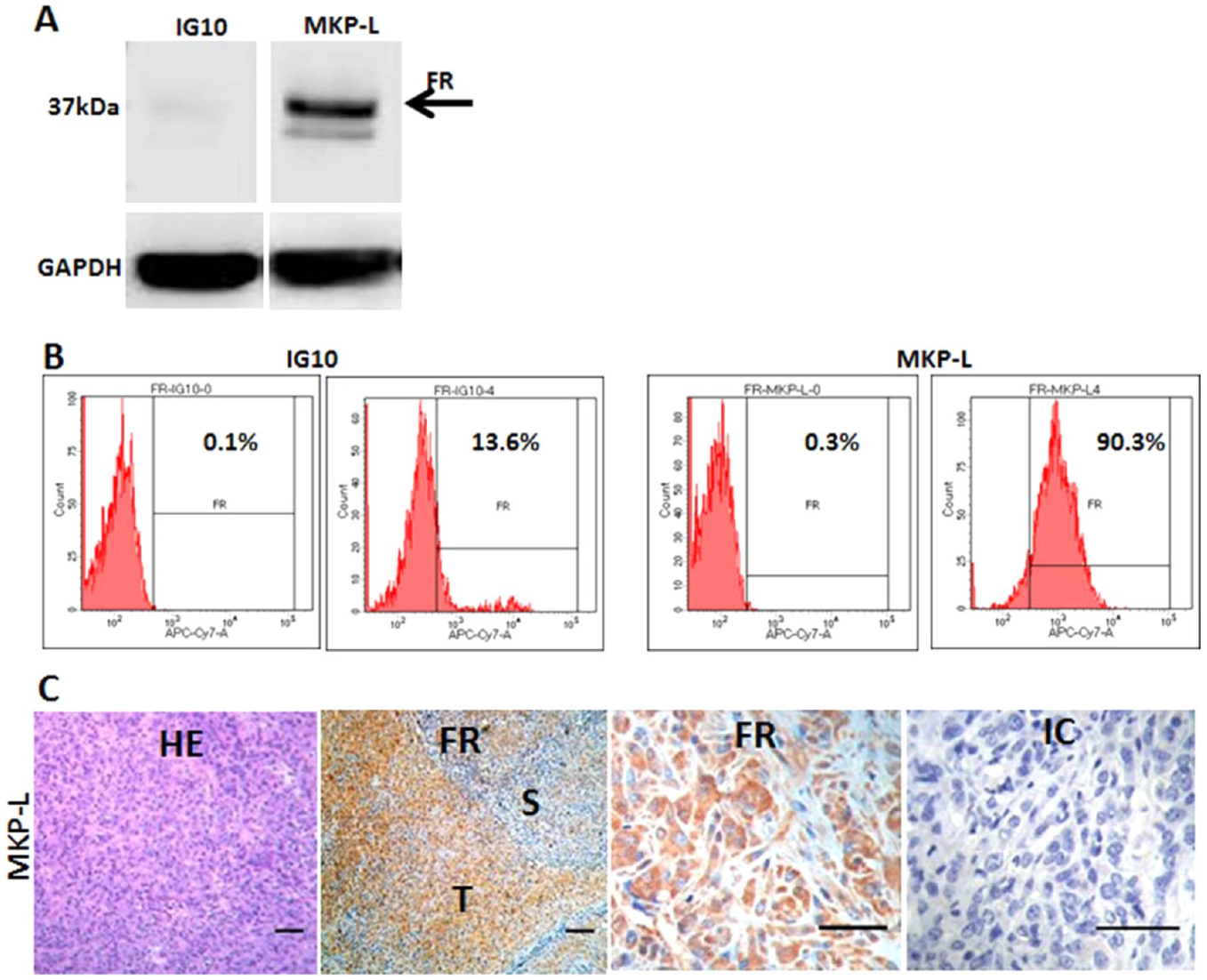

Figure 1. Folate receptor expression in MKP-L cells *in vitro* and *in vivo*. (A) FR protein expression in MKP-L cells detected by Western blot using rabbit anti-FR polyclonal antibody. Low FR expressing IG10 murine ovarian cancer cells were used as controls. Glyceraldehyde 3-phosphate dehydrogenase (GAPDH) protein levels were used as loading controls. (B) FR protein expression in IG10 (left two histograms) and MKP-L (right two histograms), detected with flow cytometry using fluorescent FR680. Cells not exposed to FR680 (autofluorescence) were used as negative controls. The gate for FR positive events was set outside of the control histogram. Background staining (0.1 and 0.3%) and the percentage of FR+ IG10 and MKP-L cells are shown (13.6 and 90.3%, respectively). The same FR680 concentration was used for both cell lines. (C) MKP-L tumor histology. Female mice were injected i.p. with 6×10^6 cells; tumors were isolated at necropsy, formalin-fixed, and paraffin embedded. Five micron sections were prepared for histology. Left panel: HE staining of a MKP-L tumor section (10×). Image shown is representative of tumors from three different mice, with at least two tumor sites sampled. Second and third panels (from left to right): IHC staining for FR (10× and 40× objectives, respectively), using anti-FR antibody. FR positive cells are shown in brown (S: stroma, T: tumor). Right panel: IHC image of one section stained with isotype control antibody. Scale bars: 100 μm.

by ethanol fixation and paraffin embedding. Four micron sections were stained for FRα expression using the same antibody as for Western blot. For detection, we employed Dako EnVision+ System-HRP labeled Polymer Anti-Rabbit (K4003) DAB substrate Kit (Abcam, ab64238). Images were captured with Zeiss camera-equipped microscope using AxioVision software.

Statistical Analysis. All data are presented as mean ± SD related with ^{68}Ga-cm09 experiments. For FMT experiments, data are presented as mean ± SE. A Student's *t* test (2-tailed, unpaired) was used to compare two data sets and *p* values less than 0.05 were considered significant. All statistical analysis was performed using PRISM software (GraphPad).

RESULTS

Transplantable Ovarian Tumor Model. The MKP-L expresses FRα, as detected by Western Blot (Figure 1A), with 90% of cells showing cell surface expression by flow cytometry (Figure 1B). This is in contrast to the low FR expression seen in immortalized IG10 murine ovarian cancer cells, derived from ovarian surface epithelial cells of healthy female mice (Figure 1A,B).[4] When injected i.p., the MKP-L cells invariably trigger widespread abdominal tumors, clinically detectable between 4 and 8 weeks following tumor cell injections. If left untreated, mice succumb to large disease burden, within approximately 8–10 weeks post-tumor challenge. Tumor implants were detected throughout the peritoneal cavity, often surrounding the major

DOI: 10.1021/mp500628g
Mol. Pharmaceutics 2015, 12, 542–553

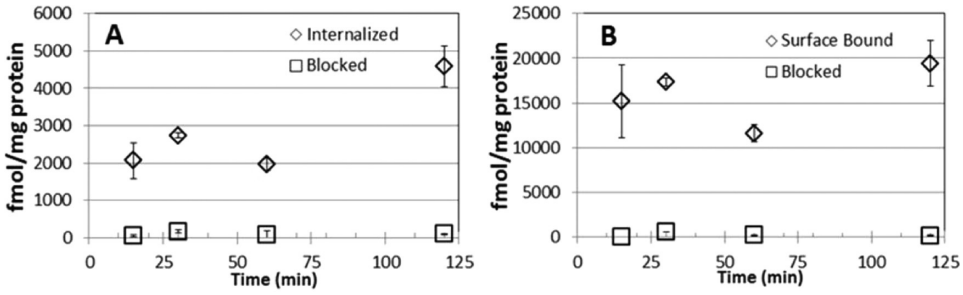

Figure 2. Internalization of ^{68}Ga-cm09 in MKP-L cells (n = 3). All data are normalized for protein content. By 2 h, the amount of ^{68}Ga-cm09 internalized reached 4587.94 ± 550.08 fmol/mg protein (A), whereas the amount of ^{68}Ga-cm09 bound to the cell surface reached 19415.90 ± 2543.50 fmol/mg protein (B). Specific receptor-mediated internalization and surface bound fraction was blocked by folic acid in the medium (p = 0.011 and p = 0.001, respectively). Error bars represent standard deviations.

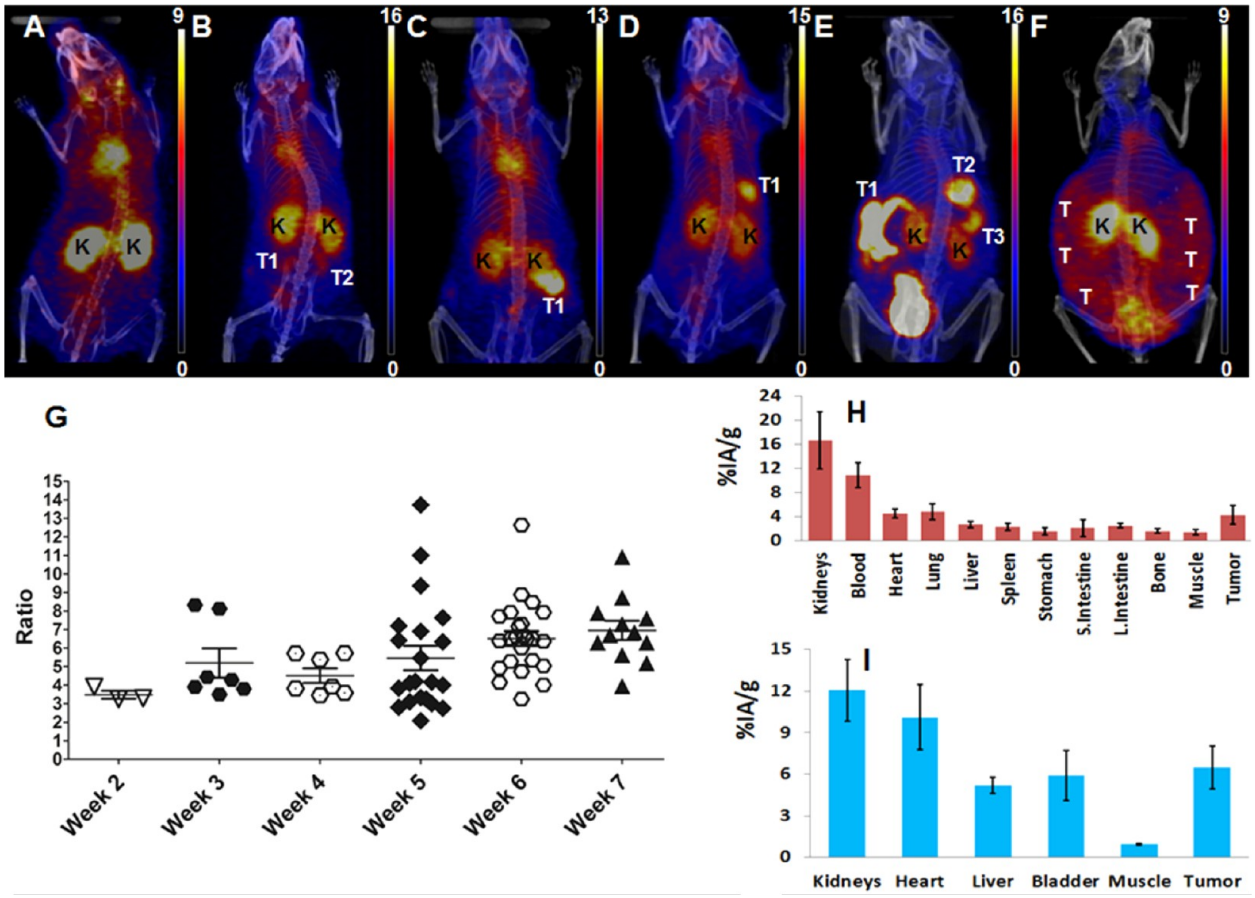

Figure 3. Detection of i.p. MKP-L tumors by ^{68}Ga-cm09 PET/CT in late stage disease in a control mouse vs 5 tumor-bearing mice (T# = tumor (and tumor index); K = kidneys), showing the various levels of disease (numbers of tumors, presence or not of ascites). All images were obtained 3−3.5 h after injection of the radiotracer. Images presented in %IA/g. Individual images are scaled based on the highest activity tumor. (A) Control mouse (Mouse 12); (B) Mouse 8, 5 weeks after MKP-L cell injection (T1 = 7.6 %IA/g, T2 = 7.7 % IA/g, K = 12.3 %IA/g); (C) Mouse 10, 7 weeks after MKP-L cell injection (T1 = 13.9 %IA/g, kidneys, K = 12.6 %IA/g); (D) Mouse 5, 6 weeks after MKP-L cell injection (T1 = 13.9 %IA/g, K = 12.5 %IA/g); (E) Mouse 1, 5 weeks after MKP-L cell injection (T1 = 15.1 %IA/g, T2 = 13.5 %IA/g, T3 = 12.1 %IA/g, K = 10.4 %IA/g); (F) Mouse 3, 5 weeks after MKP-L cell injection with ascites (tumors were dispersed throughout peritoneum and were not assigned indices, ascites activity = 6.9 %IA/g, K = 14.1 %IA/g). (G) Tumor to muscle ratios of ^{68}Ga-cm09 over time based on image ROI analysis in mice that had observable tumors at each weekly imaging session. In week 2, number of mice (N_M) = 4, number of tumors (N_T) = 3; in week 3, N_M = 4, N_T = 7; in week 4, N_M = 4, N_T = 7; in week 5, N_M = 7, N_T = 21; in week 6, N_M = 7, N_T = 24; in week 7, N_M = 3, N_T = 12. (H) Biodistribution and (I) PET/CT data in the same MKP-L-bearing mice (n = 3) injected with ^{68}Ga-cm09. The biodistribution study at 4 h postinjection (p.i.) was performed after PET/CT imaging (3 h). The PET color scales are in units of %IA/g. Error bars represent standard deviations.

organs such as the kidneys, liver, intestines, bladder, and stomach. Six of the 13 mice (46%) injected with tumor cells developed ascites 5−8 weeks after implantation (see Table S1 in Supporting Information). The tumors were FRα+, as confirmed with immunohistochemistry, demonstrating that the MKP-L cells maintained FRα expression during *in vivo* tumor formation (Figure 1C). Overall, these results validate the

DOI: 10.1021/mp500628g
Mol. Pharmaceutics 2015, 12, 542−553

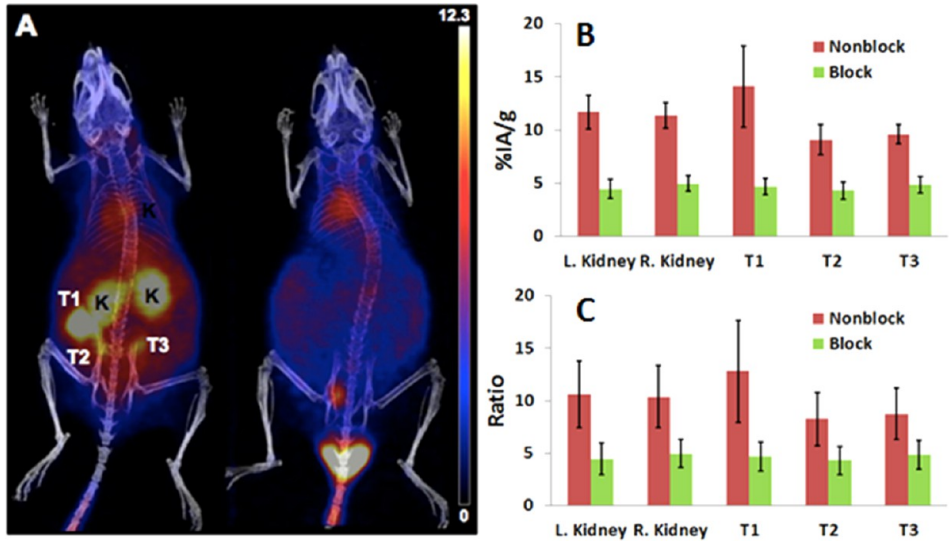

Figure 4. (A) Small animal PET/CT maximum intensity projection images of MKP-L tumor bearing mouse (Mouse 15) at 3 h post injection of ^{68}Ga-cm09 (*T*# = tumor (and tumor index). PET/CT scan of nonblocked (left) and preblocked (right) of the same mouse indicates specific tumor uptake of ^{68}Ga-cm09. Uptake in tissues is presented in units of %IA/g. The tail signal in the preblocked mouse is due to extravasation that occurred during the initial attempt of the tail vein injection. (B) PET/CT uptake at 3 h p.i. of ^{68}Ga-cm09 in the nonblocked and blocked MKP-L tumor-bearing mouse (p = 0.001). (C) PET/CT organ or tumor to muscle uptake ratios between nonblocked and blocked mouse (p = 0.002). Error bars represent standard deviations.

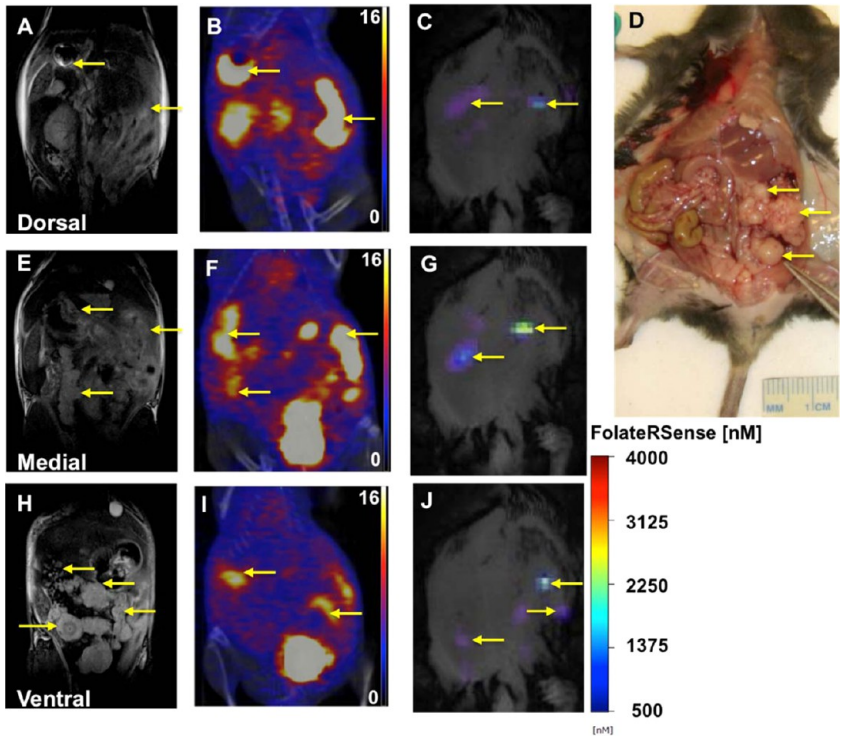

Figure 5. Coronal and dissection images of a C57BL/6 mouse (Mouse 1) sacrificed 5 weeks after MKP-L injection showing ascites and widespread i.p. tumors. Images in the top row are the most dorsal and include stomach and kidneys, middle row images are medial, and bottom row images are the most ventral and include the bladder. (A,E,H) T_2-weighted MR images. (B,F,I) PET/CT images. (C,G,J) FMT images. (D) Gross dissection of i.p. tumors. Yellow arrows indicate tumors and/or tracer uptake outside of the kidneys and bladder. The PET color scales are in units of %IA/g.

MKP-L ovarian tumor cells as a new FRα+ transplantable tumor model in immunocompetent mice.

Gallium-68 (^{68}Ga) Labeling and Internalization Assay. The internalization behavior for ^{68}Ga-cm-09 is shown in Figure 2. Six percent of the total activity/mg protein was specifically internalized after 2 h incubation time. Cell-associated activity was significantly reduced after blockade with folic acid.

PET/CT Imaging and Biodistribution Analysis. The PET/CT images of ^{68}Ga-cm09 in mice with peritoneal tumors showed high and specific uptake of ^{68}Ga-cm09 in the tumors compared to control (baseline) mice (Figures 3−6). A substantial increase in tumor uptake of ^{68}Ga-cm09 started after 2 weeks (Figures 3G and 6). Tumor progression was quantified using the %IA/g from the ROIs. Figure 3G shows

DOI: 10.1021/mp500628g
Mol. Pharmaceutics 2015, 12, 542−553

the tumor to muscle ratios of ^{68}Ga-cm09 over time. To ensure that the same tumor region was evaluated at each time point, ROIs were first defined using the scan taken at the last time point where focal uptake was obvious (7 weeks), and then an ROI of equal size was defined retrospectively for each of the earlier scans. The tumor to muscle ratios of ^{68}Ga-cm09 were 3−3.5 in the earlier weeks (Figure 3G), with a trend of increasing over the course of the disease progression. However, because of high variability at later stage disease, these changes were not statistically significant (p = 0.43). Tumors that formed in close proximity to the kidneys and bladder were not included since the high activity in normal tissues prevented accurate quantification in the tumors. Further, in some cases, increased uptake was observed in the heart and major vessels within the epigastric and superior umbilical regions. Suspicious lesions in these areas were also not included in our calculations.

The biodistribution analysis at 4 h post ^{68}Ga-cm09 injection (n = 3) immediately following PET/CT imaging showed specific accumulation (4.2 ± 1.5 %IA/g) of the radiotracer in tumors (Figure 3H,I). The highest activity for ^{68}Ga-cm09, 16.7 ± 4.7 %IA/g, was found in the kidneys. Blood had the second highest activity, 10.8 ± 2.1 %IA/g, likely due to the albumin-binding properties of cm09 that prolongs its blood circulation time. The influence of the molar amount of cm09 labeled with ^{177}Lu on tissue distribution was previously investigated.[19] There was a slight trend toward increasing accumulation of radioactivity in the blood, tumors, and kidneys as the amount of cm09 injected was increased. However, the tumor to muscle ratios also remained largely unchanged. In this study, high blood uptake might also correlate with the injected molar amount (0.5−0.8 nmol) of ^{68}Ga-cm09. However, the kidney to muscle ratio was 13.0 ± 2.6 and 12.3 ± 5.1 for PET/CT images (n = 3) and the biodistribution study (n = 3), respectively. High folate uptake in the kidney is expected due to its intrinsically high FR-expression.[8]

Since ^{68}Ga-cm09 was mostly eliminated by the kidneys, lower activity was observed in the gastrointestinal (GI) tract (the small and large intestine uptake was 2.3 ± 1.2 and 2.5 ± 0.3 %IA/g at 4 h p.i. (n = 3), respectively). Overall, tumor uptake in the same mice by ROI analysis from the PET/CT images at 3 h p.i. was higher than the biodistribution results (6.5 ± 1.5 vs 4.6 ± 1.7 %IA/g) due to partial volume effects: most tumors were localized in fatty tissues, and it was not easy to remove the tumors without including some of the surrounding fat for the biodistribution studies for total tumor quantification.

Mice receiving a blocking dose of folic acid showed a significant (p = 0.001) reduction in uptake of the ^{68}Ga-cm09 in kidneys and tumors (Figure 4) according to their baseline images, which were taken 1 day prior.

FMT Imaging. FMT of FR680 detected tumor masses as early as 2 weeks postimplantation (Figures 5−7). ROIs covering the whole abdominal region were drawn to obtain the total i.p. FR680 uptake and to account for total tumor development (Figure 7H,I). Control mice showed that FR680 uptake in mice without tumors was minimal at 6 h p.i. compared to the total fluorescence signal in the abdominal cavities of tumor-bearing mice. The total i.p. fluorescence signal in nontumor bearing mice was used to normalize the total i.p. fluorescence signal from tumor-bearing mice. The average tumor to muscle ratios throughout the study were ∼3, with no statistically significant differences in the weekly ratios (p > 0.05).

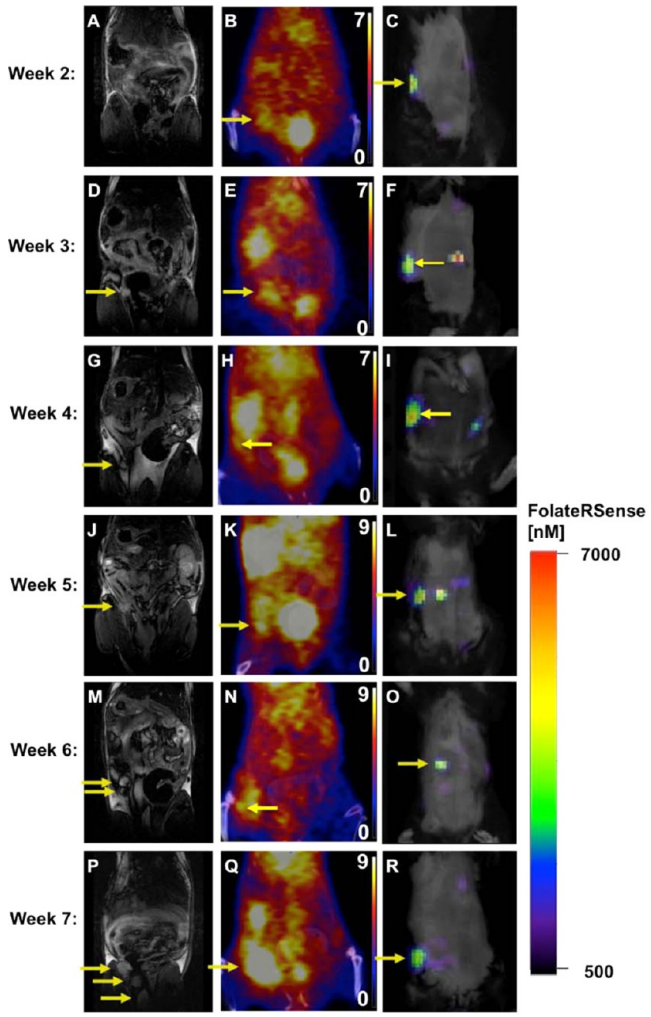

Figure 6. Coronal images of a C57BL/6 mouse (Mouse 7) 2−7 weeks after MKP-L injection before the development of ascites. (A,D,G,J,M,P) T_2-weighted MR images. (B,E,H,K,N,Q) PET/CT images. (C,F,I,L,O,R) FMT images. Yellow arrows indicate tumors and/or tracer uptake outside of the kidneys and bladder. The PET color scales are in units of %IA/g.

MRI Results. Tumors were best detected in the T_2-weighted MRIs (Figure 8), where they typically appeared to be brighter than the surrounding tissue, particularly once ascites developed (Figure 5). The T_1-VIBE images were useful for distinguishing healthy intestinal tissue from tumor tissue as the tumor tissue grew throughout the abdominal cavity and became intertwined with the intestines. Gadobenate dimeglumine administration did not enhance tumor visibility in the T_1-weighted images (Figure 8). However, interstitial fluid in the peritoneum was brightened in the p.i. images. Tumors in the peritoneal cavity were visible in MR images at 3 weeks post-tumor cell injection (Figure 6).

Multimodal Imaging. Cohort 2 was imaged every week starting at 2 weeks p.i. of MKP-L cells by MRI, small animal PET/CT, and FMT (Figure 6). Tumors were visible by all three modalities with varying sensitivity and anatomical resolution. The growth of individual tumor regions was monitored over time. In one example (Figure 6), the tumor was initially visualized at 2 weeks postimplantation by PET/CT and FMT imaging and at 3−4 weeks by MRI. However, in another representative mouse (Figure 5), there were four

DOI: 10.1021/mp500628g
Mol. Pharmaceutics 2015, 12, 542−553

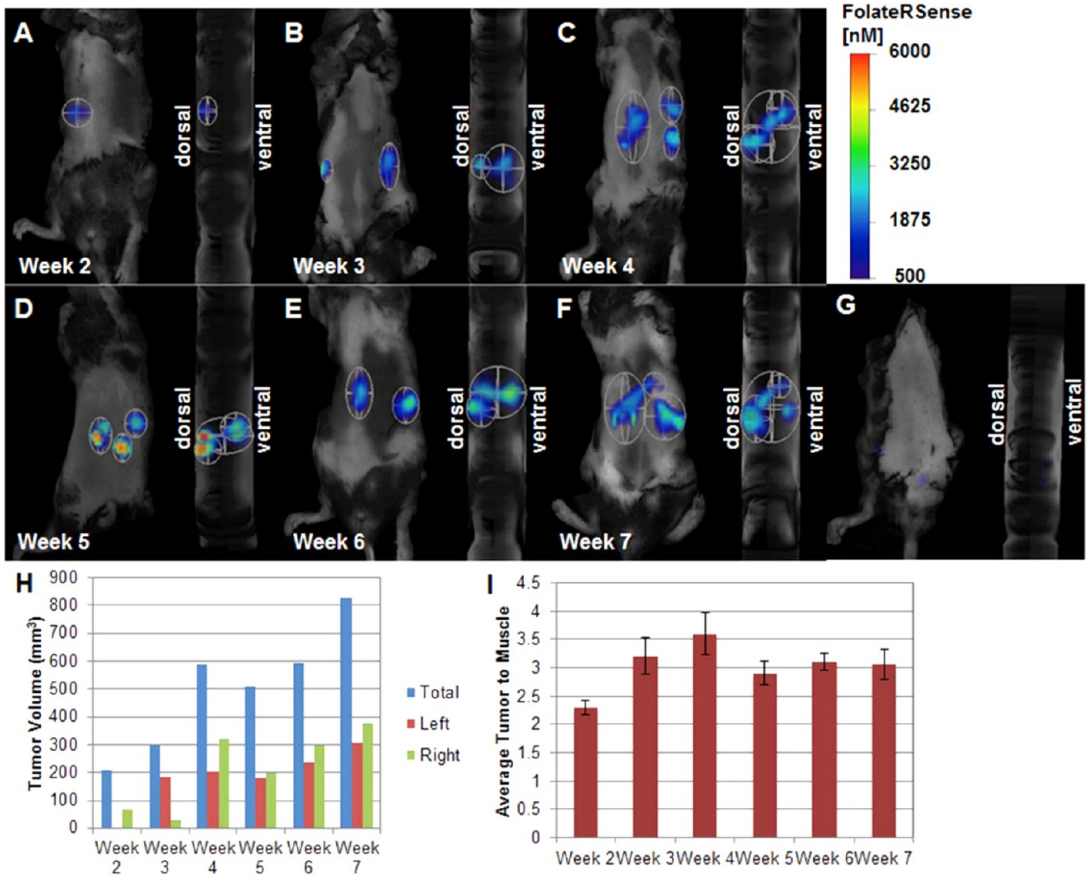

Figure 7. FMT imaging of MKP-L tumors. (A–F) FMT images of a tumor-bearing mouse (Mouse 10) injected with 2 nmol FR680 at 2–7 weeks post-tumor implantation show the development of tumors in the i.p. cavity. (G) FMT images of a nontumor-bearing mouse injected with 2 nmol FR680. (H) Tumor volumes in Mouse 10 over time. Blue bars represent total tumor volume in the i.p. cavity, red bars represent tumor volume in the left side of the i.p. cavity, and green bars represent tumor volume in the right side of the i.p. cavity. (I) Tumor to muscle ratios of quantified FR680 fluorescence signal in the i.p. cavity over time. Error bars represent standard error.

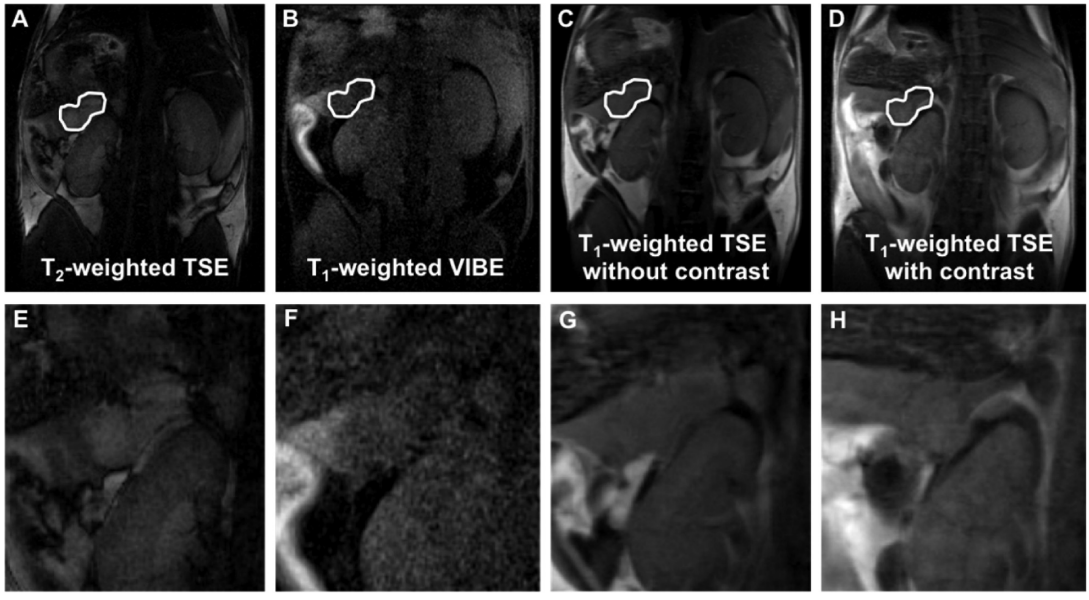

Figure 8. MRI images of a periadrenal tumor at 6 weeks (Mouse 10) after induction taken with different imaging sequences. (A) T_2-weighted turbo spin echo (TSE), (B) T_1-weighted volume interpolated gradient echo (VIBE), which makes intestinal tissue appear bright white, (C) T_1-weighted TSE, and (D) T_1-weighted TSE after the administration of a gadolinium-based contrast agent. The tumor area is outlined in white. (E–H) Magnified images showing the periadrenal tumors and surrounding adrenal and intestinal tissue.

DOI: 10.1021/mp500628g
Mol. Pharmaceutics 2015, 12, 542–553

tumors that were clearly observed by 5 weeks postimplantation by all three imaging modalities.

DISCUSSION

The clinical management of EOC will benefit from diagnostic techniques that can detect primary tumors in the early stages and monitor recurrent disease. Herein, we describe a novel FRα+ transplantable EOC mouse model that mimics a recurrent form of human disease. We evaluated the effectiveness of multimodal imaging for the early detection of peritoneal tumor implants in an immunocompetent host using FR-targeted imaging agents. Our EOC mouse model is easy to produce and has a yield approaching 100%. Similarly, transplantation of the BRCA1-deficient BR5 cell line in FVB/NJ mice produces intraperitoneal tumors.[29] The BR5 cell line was also found to have high FR-expression. The MKP cells derive from an animal with MUC1 overexpression, which occurs in ~90% of human EOC and only 5% of normal ovarian tissue.[28,30] By contrast, BRCA1 mutations are only responsible for ~10% of EOC.[31]

However, not all human or murine ovarian cancer cell lines have significant FR-expression. Indeed, we found that with the exception of the MKP-L cell line, most of the MKP cell line variants had low FR expression.

Intraperitoneal MKP-L tumors were detected by all three imaging modalities. Overall, PET/CT and FMT molecular imaging detected FRα+ tumor tissue as early as 2 weeks after tumor cell implantation (Figure 6). MRI had the highest anatomical resolution of the three modalities, but its utility was limited by the lack of a FR-targeted reporter. Co-registration of the images was challenging despite the availability of a multimodality animal imaging cassette (PerkinElmer). The FMT and PET/CT scans had to be conducted on different days to avoid the competition of the different reporters for FRs so positioning of the animal varied between scans. The cassette is poorly suited for MRI since it requires the MRI receiver coil to be placed outside of the cassette, centimeters away from the animal, resulting in significant signal loss. Ideally, the structural and molecular images should be acquired during the same exam, e.g., using PET/CT or PET/MRI to facilitate image coregistration and maximize the diagnostic benefit.

PET imaging is used in both preclinical and clinical settings to noninvasively study the molecular basis of disease and to guide the development of novel molecular-based treatments.[32] Clinical PET has superior sensitivity and resolution versus SPECT.[33] Small animal PET imaging is able to quantify radiotracer uptake within lesions with a resolution of <2 mm and a remarkably high reporter sensitivity of up to 10^{-11}–10^{-12} mol/L.[34] Previously reported folate-based radiopharmaceuticals developed for PET imaging show rapid clearance from blood circulation, which results in low background organ exposure and enhances tumor to blood activity ratios.[35−39] However, these pharmacokinetic properties also lead to low uptake in tumor tissue and high accumulation of radioactivity in the kidneys.[35,37−39] To overcome this issue, Müller et al.[19] designed a folate conjugate, DOTA-folate (cm09), with an albumin-binding entity to prolong circulation in the blood and improve tumor to kidney ratios. The conjugate cm09 was labeled with the longer-lived beta emitting radionuclide, ^{177}Lu, and the resulting agent showed therapeutic efficacy in a FRα+ tumor-bearing mouse model.[19] The conjugate cm09 was subsequently radiolabeled with ^{44}Sc ($t_{1/2}$ = 3.97 h, $E_{average}\beta^+$ = 0.632 MeV, 94.3%) for PET imaging.[21]

Here we set out to determine whether ^{68}Ga-cm09 would visualize orthotopic FRα+ ovarian tumors by PET imaging. The physical 68 min half-life of ^{68}Ga is shorter than the 4 h biological half-life of cm09 in blood. However, our imaging results indicate that the half-life of ^{68}Ga is sufficient for FR-imaging in our model and should result in lower radiation dose than ^{44}Sc *in vivo*. ^{64}Cu ($t_{1/2}$ = 12.70 h, $E_{average}\beta^+$ = 0.653 MeV) and ^{89}Zr ($t_{1/2}$ = 3.27 days, $E_{average}\beta^+$ = 0.389 MeV) would make attractive PET nuclides for radiolabeling the albumin-binding folate agent if the DOTA chelator was replaced with either a NODAGA (^{64}Cu) or a desferrioxamine (^{89}Zr) chelator to allow the formation of stable complexes.[40,41]

FR binding studies with KB cells were previously conducted using radiolabeled cm09 and its predecessor, ^{67}Ga-DOTA-Bz-EDA-folate (without the albumin binder).[21,36] These studies showed cell binding of 40−70% and internalization of ~20% at 120 min p.i. Our study showed cell binding and internalization of 25% and 6% IA/mg protein, respectively. Blocking with folic acid resulted in negligible uptake and internalization for all studies. Therefore, the ratio of internalization/cell binding was higher for the KB cells compared with the MKP-L. However, KB cells have 2−10 times higher FR-expression than serous and metastatic ovarian tumors.[7,8]

We did not conduct uptake studies using the FR680 optical tracer. Studies by PerkinElmer showed high uptake in KB cells and a dissociation constant (K_d) of 5 nM.[42] *In vivo*, the concentration of FR680 in KB xenografts was 400 pmol at 4 h after injection of 2 nmol FR680. Blocking with folic acid reduced uptake by 99% and 80% *in vitro* and *in vivo*, respectively.

^{68}Ga-cm09 has the advantage of lower kidney uptake (16.65 ± 4.74% IA/g at 4 h p.i.) compared to the previously reported, more rapidly clearing $^{68/67}$Ga tracers (130.31 ± 14.65 vs 111.96 ± 15.33 %IA/g at 4 h p.i. reported for $^{68/67}$Ga−P3246 and $^{68/67}$Ga−P3238; 103.01 ± 24.58 vs 103.95 ± 16.96 %IA/g at 4 h p.i. reported for $^{68/67}$Ga−P3026 and $^{68/67}$Ga−P1254; and 84.53 ± 14.10 %IA/g at 4 h p.i. for ^{67}Ga-DOTA-Bz-EDA-folate).[36−38] Even though ^{68}Ga-cm09 cleared slowly from the blood, there was still good visualization of the orthotopic MKP-L tumors even in mice that had intermittent folate in their diet.

Optical imaging is widely used in preclinical studies and increasingly in clinical settings for intraoperative fluorescence image guided surgery.[12,43] While FMT is limited by the diffusive nature of near-infrared (NIR) photons that limit depth penetration to a few centimeters, FMT imaging systems enable noninvasive, quantitative molecular imaging of small animals without the use of ionizing radiation.[44] The FMT2500 system used in the present study has a low reporter threshold for detection (down to 1 pmol), similar to PET with comparable spatial resolution (>1 mm). However, FMT has the ability to image multiple tracers at the same time.[45]

High-field MRI is commonly used in small animal imaging to detect and characterize tumors throughout the body in addition to its clinical applications.[46] In this study, T_2-weighted images readily revealed tumor tissue at the middle stage of the disease starting at approximately 4 weeks after implantation.

Several MRI reporters are available that can bind to tumor-specific receptors and enhance visibility.[47,48] The present study utilized nonspecific gadobenate dimeglumine, which alters the relaxation times of water molecules in intravascular and extracellular spaces, typically leading to enhanced visibility of tumors and lesions. However, in the imaging of the EOC mouse model, gadobenate dimeglumine did not enhance tumor

DOI: 10.1021/mp500628g
Mol. Pharmaceutics 2015, 12, 542−553

visibility. Folate receptor targeted MRI contrast agents based on magnetic nanoparticles (MNPs) are commercially available (e.g., Nanopartz) for use in preclinical models. However, the MNPs produce hypointense signals using T_2- or T_2*-weighted MRI that are difficult to discern from abdominal tissues such as bowel.

In this study, the three different imaging modalities were combined to overcome the limitations of the individual techniques to detect tumor tissue as early as 2 weeks postimplantation of MKP-L cells. Because of the lack of an anatomical imaging technique and the diffusive nature of light, FMT displayed the lowest anatomical resolution of the three imaging modalities. Incorporation of another imaging modality, such as MRI, and coregistration of the images would benefit both modalities. Second, while tumors are well visualized using PET/CT, high renal uptake limits tumor delineation near the kidneys. In this study, we used the albumin-binding capabilities of cm09 to significantly reduce renal uptake. High renal uptake of conventional folate radioconjugates can also be reduced by using antifolates without impacting tumor uptake.[49] In the present study, the lower amount of renal and bladder uptake in the FMT images versus PET images during the same week greatly improved the quality of the images around these organs. The molecular structure of the FR680 tracer is proprietary, and therefore, we do not know how uptake in the normal tissues was minimized.

Third, MRI has superior anatomical resolution to PET and FMT. However, the lack of a useful FR-targeted MRI reporter limited the detection of tumor to 4 weeks post-tumor implantation compared to 2 weeks for PET and FMT. Nevertheless, MRI can also provide valuable structural and functional information in the early stages of tumors that are detected using PET/CT or optical. Diffusion weighted imaging (DWI) MRI may be useful for detecting ovarian tumors *in vivo* based on the reduced apparent diffusion coefficient (ADC) values in the tumor relative to normal tissues.[50] However, DWI is vulnerable to physiological motion present in the abdomen.[51] The employment of FR-targeted fluorescence and PET imaging agents in combination with MRI (e.g., PET/MRI) can lead to higher sensitivity than each modality, potentially resulting in the diagnosis of "low volume," early stage EOC.[52]

The overexpression of MUC1 and FRα in most ovarian cancers combined with their limited expression in healthy tissues make them an attractive tumor-associated molecular target in imaging and therapy. Noninvasive imaging of FRα+ cells using highly selective and specific folate conjugates and sensitive molecular imaging will be of great utility in clinical ovarian cancer management. The results of this study make a strong case for multimodal imaging in preclinical ovarian cancer models. Moreover, we have demonstrated that our new ovarian tumor model in immunocompetent mice emulates the human disease by reliably inducing widespread i.p. tumors marked by overexpression of FRα.

■ ASSOCIATED CONTENT

Ⓢ Supporting Information

Table S1. Summary of experimental schema. This material is available free of charge via the Internet at http://pubs.acs.org.

■ AUTHOR INFORMATION

Corresponding Author

*Phone: (412) 864-1653. Fax: (412) 647-9800. E-mail: gach@pitt.edu.

Author Contributions

○These authors contributed equally. The manuscript was written through contributions of all authors. All authors have given approval to the final version of the manuscript.

Notes

The authors declare no competing financial interest.

■ ACKNOWLEDGMENTS

The authors thank Kathryn Day, Emre Demirci, and Joseph D. Latoche for technical help (PET/CT imaging) and Jalpa Modi (cell culture work). The authors also thank Sandra Orsulic for access to the BR5 cell line and her years of technical guidance and enthusiastic support. The authors thank the reviewers for their constructive inputs. This project was funded by National Cancer Institute (NCI) grant R01CA163462, Department of Defense Ovarian Cancer Academy Award grant W81XWH-10-1-0525, the University of Pittsburgh's Department of Radiology, and a University of Pittsburgh Cancer Institute (UPCI) Pilot Award. The imaging studies used the UPCI Animal Facility and In Vivo Imaging Facility that are supported in part by NCI grant P30CA047904.

■ ABBREVIATIONS

ADC, apparent diffusion coefficient; CT, computed tomography; DAB, 3,3′-diaminobenzidine; DMEM, Dulbecco's modified eagle medium; DOTA, 1,4,7,10-tetraazacyclododecane-1,4,7,10-tetraacetic acid; DTT, dithiothreitol; DWI, diffusion weighted imaging; EOC, epithelial ovarian cancer; FBS, fetal bovine serum; FFRPMI, folate-free RPMI; FLASH, fast low angle shot; FMT, fluorescence molecular tomography; FR, folate receptor; FRα, folate receptor α; ^{68}Ga, gallium 68; GAPDH, glyceraldehyde 3-phosphate dehydrogenase; Gd, gadolinium; HRP, horseradish peroxidase; i.p., intraperitoneal; %IA/g, percent injected activity per gram; IgG, immunoglobulin G; IRW, Inveon research workplace; MBq, megaBecquerel; MKP, MUC1KrasPten; MNP, magnetic nanoparticle; MRI, magnetic resonance imaging; NaOAC, sodium acetate; NODAGA, a NOTA-derived chelator; NOTA, 1,4,7-triazacyclononane-triacetic acid; p.i., postinjection; PAGE, polyacrylamide gel electrophoresis; PBS, phosphate-buffered saline; PET, positron emission tomography; PSG, penicillin−streptomycin−glutamine; ROI, region of interest; RP-HPLC, reversed-phase high-performance liquid chromatography; s.c., subcutaneous; SD, standard deviation; SDS, sodium dodecyl sulfate; SE, standard error; SPECT, single photon emission computed tomography; T, tesla; $t_{1/2}$, half-life; Tc, technetium; TE, echo time; TR, repeat time; TSE, turbo spin echo; VIBE, volumetric interpolated breath hold examination

■ REFERENCES

(1) Mantia-Smaldone, G. M.; Edwards, R. P.; Vlad, A. M. Targeted treatment of recurrent platinum-resistant ovarian cancer: current and emerging therapies. *Cancer Manag. Res.* **2011**, *3*, 25−38.

(2) Cho, K. R.; Shih, M. Ovarian cancer. *Annu. Rev. Pathol.* **2009**, *4*, 287−313.

(3) House, C. D.; Hernandez, L.; Annunziata, C. M. Recent technological advances in using mouse models to study ovarian cancer. *Front. Oncol.* **2014**, *4*, 26.

(4) Roby, K. F.; Taylor, C. C.; Sweetwood, J. P.; Cheng, Y.; Pace, J. L.; Tawfik, O.; Persons, D. L.; Smith, P. G.; Terranova, P. F. Development of a syngeneic mouse model for events related to ovarian cancer. *Carcinogenesis* **2000**, *21* (4), 585−91.

DOI: 10.1021/mp500628g
Mol. Pharmaceutics 2015, 12, 542−553

(5) Xing, D.; Orsulic, S. A mouse model for the molecular characterization of brca1-associated ovarian carcinoma. *Cancer Res.* **2006**, *66* (18), 8949−53.
(6) Kalli, K. R.; Oberg, A. L.; Keeney, G. L.; Christianson, T. J. H.; Low, P. S.; Knutson, K. L.; Hartmann, L. C. Folate receptor alpha as a tumor target in epithelial ovarian cancer. *Gynecol. Oncol.* **2008**, *108* (3), 619−626.
(7) Weitman, S. D.; Lark, R. H.; Coney, L. R.; Fort, D. W.; Frasca, V.; Zurawski, V. R., Jr.; Kamen, B. A. Distribution of the folate receptor GP38 in normal and malignant cell lines and tissues. *Cancer Res.* **1992**, *52* (12), 3396−401.
(8) Parker, N.; Turk, M. J.; Westrick, E.; Lewis, J. D.; Low, P. S.; Leamon, C. P. Folate receptor expression in carcinomas and normal tissues determined by a quantitative radioligand binding assay. *Anal. Biochem.* **2005**, *338* (2), 284−93.
(9) Low, P. S.; Henne, W. A.; Doorneweerd, D. D. Discovery and development of folic-acid-based receptor targeting for imaging and therapy of cancer and inflammatory diseases. *Acc. Chem. Res.* **2008**, *41* (1), 120−9.
(10) Clifton, G. T.; Sears, A. K.; Clive, K. S.; Holmes, J. P.; Mittendorf, E. A.; Ioannides, C. G.; Ponniah, S.; Peoples, G. E. Folate receptor alpha: a storied past and promising future in immunotherapy. *Hum Vaccin.* **2011**, *7* (2), 183−90.
(11) Vlahov, I. R.; Leamon, C. P. Engineering folate-drug conjugates to target cancer: from chemistry to clinic. *Bioconjugate Chem.* **2012**, *23* (7), 1357−69.
(12) van Dam, G. M.; Themelis, G.; Crane, L. M.; Harlaar, N. J.; Pleijhuis, R. G.; Kelder, W.; Sarantopoulos, A.; de Jong, J. S.; Arts, H. J.; van der Zee, A. G.; Bart, J.; Low, P. S.; Ntziachristos, V. Intraoperative tumor-specific fluorescence imaging in ovarian cancer by folate receptor-alpha targeting: first in-human results. *Nat. Med.* **2011**, *17* (10), 1315−9.
(13) Müller, C. Folate based radiopharmaceuticals for imaging and therapy of cancer and inflammation. *Curr. Pharm. Des.* **2012**, *18* (8), 1058−83.
(14) Leamon, C. P.; Parker, M. A.; Vlahov, I. R.; Xu, L. C.; Reddy, J. A.; Vetzel, M.; Douglas, N. Synthesis and biological evaluation of EC20: a new folate-derived, ^{99m}Tc-based radiopharmaceutical. *Bioconjugate Chem.* **2002**, *13* (6), 1200−10.
(15) Reddy, J. A.; Allagadda, V. M.; Leamon, C. P. Targeting therapeutic and imaging agents to folate receptor positive tumors. *Curr. Pharm. Biotechnol.* **2005**, *6* (2), 131−50.
(16) Dixit, V.; Van den Bossche, J.; Sherman, D. M.; Thompson, D. H.; Andres, R. P. Synthesis and grafting of thioctic acid-PEG-folate conjugates onto Au nanoparticles for selective targeting of folate receptor-positive tumor cells. *Bioconjugate Chem.* **2006**, *17* (3), 603−9.
(17) Fisher, R. E.; Siegel, B. A.; Edell, S. L.; Oyesiku, N. M.; Morgenstern, D. E.; Messmann, R. A.; Amato, R. J. Exploratory study of ^{99m}Tc-EC20 imaging for identifying patients with folate receptor-positive solid tumors. *J. Nucl. Med.* **2008**, *49* (6), 899−906.
(18) Matteson, E. L.; Lowe, V. J.; Prendergast, F. G.; Crowson, C. S.; Moder, K. G.; Morgenstern, D. E.; Messmann, R. A.; Low, P. S. Assessment of disease activity in rheumatoid arthritis using a novel folate targeted radiopharmaceutical Folatescan. *Clin. Exp. Rheumatol.* **2009**, *27* (2), 253−9.
(19) Müller, C.; Struthers, H.; Winiger, C.; Zhernosekov, K.; Schibli, R. DOTA conjugate with an albumin-binding entity enables the first folic acid-targeted ^{177}Lu-radionuclide tumor therapy in mice. *J. Nucl. Med.* **2013**, *54* (1), 124−31.
(20) Chopra, A. [$^{149/152/155/161}$Tb]-Labeled DOTA-folate conjugated to an albumin-binding entity [$^{149/152/155/161}$Tb]cm09. In *Molecular Imaging and Contrast Agent Database (MICAD)*, December 27, 2012 ed.; National Institutes of Health: Bethesda, MD, 2012.
(21) Müller, C.; Bunka, M.; Reber, J.; Fischer, C.; Zhernosekov, K.; Türler, A.; Schibli, R. Promises of cyclotron-produced ^{44}Sc as a diagnostic match for trivalent beta−emitters: in vitro and in vivo study of a ^{44}Sc-DOTA-folate conjugate. *J. Nucl. Med.* **2013**, *54* (12), 2168−74.
(22) Novell, A.; Escoffre, J.-M.; Bouakaz, A. Ultrasound contrast imaging in cancer − Technical aspects and prospects. *Curr. Mol. Imaging* **2014**, *2* (1), 77−88.
(23) Partovi, S.; Kohan, A.; Rubbert, C.; Vercher-Conejero, J. L.; Gaeta, C.; Yuh, R.; Zipp, L.; Herrmann, K. A.; Robbin, M. R.; Lee, Z.; Muzic, R. F., Jr.; Faulhaber, P.; Ros, P. R. Clinical oncologic applications of PET/MRI: a new horizon. *Am. J. Nucl. Med. Mol. Imaging* **2014**, *4* (2), 202−12.
(24) Konda, S. D.; Aref, M.; Wang, S.; Brechbiel, M.; Wiener, E. C. Specific targeting of folate-dendrimer MRI contrast agents to the high affinity folate receptor expressed in ovarian tumor xenografts. *MAGMA* **2001**, *12* (2−3), 104−13.
(25) Topete, A.; Alatorre-Meda, M.; Villar-Alvarez, E. M.; Carregal-Romero, S.; Barbosa, S.; Parak, W. J.; Taboada, P.; Mosquera, V. Polymeric-gold nanohybrids for combined imaging and cancer therapy. *Adv. Healthcare Mater.* **2014**, *3* (8), 1309−1325.
(26) Dobrucki, L. W.; Sinusas, A. J. Cardiovascular molecular imaging. *Semin. Nucl. Med.* **2005**, *35* (1), 73−81.
(27) Kurdziel, K. A.; Lindenberg, L.; Mena, E.; Turkbey, B.; Choyke, P. The role of PET/CT and SPECT/CT in oncology drug development. *Curr. Mol. Imaging* **2014**, *2* (1), 42−52.
(28) Budiu, R. A.; Elishaev, E.; Brozick, J.; Lee, M.; Edwards, R. P.; Kalinski, P.; Vlad, A. M. Immunobiology of human mucin 1 in a preclinical ovarian tumor model. *Oncogene* **2013**, *32* (32), 3664−75.
(29) Goldberg, M. S.; Xing, D.; Ren, Y.; Orsulic, S.; Bhatia, S. N.; Sharp, P. A. Nanoparticle-mediated delivery of siRNA targeting Parp1 extends survival of mice bearing tumors derived from Brca1-deficient ovarian cancer cells. *Proc. Natl. Acad. Sci. U. S. A.* **2011**, *108* (2), 745−50.
(30) Wang, L.; Ma, J.; Liu, F.; Yu, Q.; Chu, G.; Perkins, A. C.; Li, Y. Expression of MUC1 in primary and metastatic human epithelial ovarian cancer and its therapeutic significance. *Gynecol. Oncol.* **2007**, *105* (3), 695−702.
(31) Antoniou, A.; Pharoah, P. D.; Narod, S.; Risch, H. A.; Eyfjord, J. E.; Hopper, J. L.; Loman, N.; Olsson, H.; Johannsson, O.; Borg, A.; Pasini, B.; Radice, P.; Manoukian, S.; Eccles, D. M.; Tang, N.; Olah, E.; Anton-Culver, H.; Warner, E.; Lubinski, J.; Gronwald, J.; Gorski, B.; Tulinius, H.; Thorlacius, S.; Eerola, H.; Nevanlinna, H.; Syrjakoski, K.; Kallioniemi, O. P.; Thompson, D.; Evans, C.; Peto, J.; Lalloo, F.; Evans, D. G.; Easton, D. F. Average risks of breast and ovarian cancer associated with BRCA1 or BRCA2 mutations detected in case series unselected for family history: a combined analysis of 22 studies. *Am. J. Hum. Genet.* **2003**, *72* (5), 1117−30.
(32) Levin, C. S. New imaging technologies to enhance the molecular sensitivity of positron emission tomography. *Proc. IEEE* **2008**, *96* (3), 439−467.
(33) Rahmim, A.; Zaidi, H. PET versus SPECT: strengths, limitations and challenges. *Nucl. Med. Commun.* **2008**, *29* (3), 193−207.
(34) Lecchi, M.; Ottobrini, L.; Martelli, C.; Del Sole, A.; Lucignani, G. Instrumentation and probes for molecular and cellular imaging. *Q. J. Nucl. Med. Mol. Imaging* **2007**, *51* (2), 111−26.
(35) Sega, E.; Low, P. Tumor detection using folate receptor-targeted imaging agents. *Cancer Metastasis Rev.* **2008**, *27* (4), 655−664.
(36) Müller, C.; Vlahov, I. R.; Santhapuram, H. K.; Leamon, C. P.; Schibli, R. Tumor targeting using ^{67}Ga-DOTA-Bz-folate: investigations of methods to improve the tissue distribution of radiofolates. *Nucl. Med. Biol.* **2011**, *38* (5), 715−23.
(37) Fani, M.; Tamma, M. L.; Nicolas, G. P.; Lasri, E.; Medina, C.; Raynal, I.; Port, M.; Weber, W. A.; Maecke, H. R. In vivo imaging of folate receptor positive tumor xenografts using novel ^{68}Ga-NODAGA-folate conjugates. *Mol. Pharmaceutics* **2012**, *9* (5), 1136−45.
(38) Fani, M.; Wang, X.; Nicolas, G.; Medina, C.; Raynal, I.; Port, M.; Maecke, H. R. Development of new folate-based PET radiotracers: preclinical evaluation of ^{68}Ga-DOTA-folate conjugates. *Eur. J. Nucl. Med. Mol. Imaging* **2011**, *38* (1), 108−19.
(39) Müller, C.; Schibli, R. Folic acid conjugates for nuclear imaging of folate receptor-positive cancer. *J. Nucl. Med.* **2011**, *52* (1), 1−4.

DOI: 10.1021/mp500628g
Mol. Pharmaceutics 2015, 12, 542−553

(40) Zhou, Y.; Baidoo, K. E.; Brechbiel, M. W. Mapping biological behaviors by application of longer-lived positron emitting radionuclides. *Adv. Drug Delivery Rev.* **2013**, *65* (8), 1098−111.
(41) Heneweer, C.; Holland, J. P.; Divilov, V.; Carlin, S.; Lewis, J. S. Magnitude of enhanced permeability and retention effect in tumors with different phenotypes: ^{89}Zr-albumin as a model system. *J. Nucl. Med.* **2011**, *52* (4), 625−33.
(42) Groves, K.; Bao, B.; Zhang, J.; Cuneo, G.; Yared, W.; Rajopadhye, M.; Peterson, J. D., Quantitative assessment of folate receptor expression by FMT imaging of mouse tumor xenografts with a near-infrared fluorescent folate agent. In *World Molecular Imaging Conference*, Dublin, 2012; p 1396319.
(43) James, M. L.; Gambhir, S. S. A molecular imaging primer: modalities, imaging agents, and applications. *Physiol. Rev.* **2012**, *92* (2), 897−965.
(44) Nahrendorf, M.; Keliher, E.; Marinelli, B.; Waterman, P.; Feruglio, P. F.; Fexon, L.; Pivovarov, M.; Swirski, F. K.; Pittet, M. J.; Vinegoni, C.; Weissleder, R. Hybrid PET-optical imaging using targeted probes. *Proc. Natl. Acad. Sci. U.S.A.* **2010**, *107* (17), 7910−5.
(45) Vasquez, K. O.; Casavant, C.; Peterson, J. D. Quantitative whole body biodistribution of fluorescent-labeled agents by non-invasive tomographic imaging. *PLoS One* **2011**, *6* (6), e20594.
(46) Borges, A. R.; Lopez-Larrubia, P.; Marques, J. B.; Cerdan, S. G. MR imaging features of high-grade gliomas in murine models: how they compare with human disease, reflect tumor biology, and play a role in preclinical trials. *Am. J. Neuroradiol.* **2012**, *33* (1), 24−36.
(47) Vargas, H. A.; Barrett, T.; Sala, E. MRI of ovarian masses. *J. Magn. Reson. Imaging* **2013**, *37* (2), 265−81.
(48) Mody, V. V.; Nounou, M. I.; Bikram, M. Novel nanomedicine-based MRI contrast agents for gynecological malignancies. *Adv. Drug Delivery Rev.* **2009**, *61* (10), 795−807.
(49) Müller, C.; Schibli, R.; Krenning, E. P.; de Jong, M. Pemetrexed improves tumor selectivity of ^{111}In-DTPA-folate in mice with folate receptor-positive ovarian cancer. *J. Nucl. Med.* **2008**, *49* (4), 623−9.
(50) Levy, A.; Medjhoul, A.; Caramella, C.; Zareski, E.; Berges, O.; Chargari, C.; Boulet, B.; Bidault, F.; Dromain, C.; Balleyguier, C. Interest of diffusion-weighted echo-planar MR imaging and apparent diffusion coefficient mapping in gynecological malignancies: a review. *J. Magn. Reson. Imaging* **2011**, *33* (5), 1020−7.
(51) Lee, H. J.; Luci, J. J.; Tantawy, M. N.; Lee, H.; Nam, K. T.; Peterson, T. E.; Price, R. R. Detecting peritoneal dissemination of ovarian cancer in mice by DWIBS. *Magn. Reson. Imaging* **2013**, *31* (2), 227−34.
(52) Palm, S.; Enmon, R. M., Jr.; Matei, C.; Kolbert, K. S.; Xu, S.; Zanzonico, P. B.; Finn, R. L.; Koutcher, J. A.; Larson, S. M.; Sgouros, G. Pharmacokinetics and biodistribution of ^{86}Y-trastuzumab for ^{90}Y dosimetry in an ovarian carcinoma model: correlative MicroPET and MRI. *J. Nucl. Med.* **2003**, *44* (7), 1148−55.

DOI: 10.1021/mp500628g
Mol. Pharmaceutics 2015, 12, 542−553